Population, alignment, and coherence of the foil-excited $n=2$ hydrogen atoms: Polarization observation of the field-dependent quantum beats in the Lyman-α line

Yasuyuki Kimura, Tetsuo Nishida, and Keishi Ishii

Department of Engineering Physics and Mechanics, Faculty of Engineering, Kyoto University, Kyoto 606-01, Japan

We have developed an experimental method for determining the initial density matrix of the foil-excited atoms. The excited hydrogen ($n=2$) atoms pass through a region of a variable electric field (-200 kV/m to $+200$ kV/m), and the intensity of the Lyman-α line (121.6 nm) emitted in a free space downstream is observed. By using a vacuum ultraviolet polarizer, the dependence of the intensities of the polarized components on the electric field, including the field-dependent quantum beats, was measured and it was numerically fitted to a calculation. Thus all the initial density matrix elements were determined in a single measurement. It was found that, in the energy range 100–180 keV, just after the excitation, the electron cloud has higher density in the front side of the ion and the electron probability current is backwards. [S1050-2947(97)06911-4]

PACS number(s): 34.50.Fa, 32.60.+i, 42.50.Md, 33.20.Ni

I. INTRODUCTION

In an anisotropic and instantaneous excitation of atoms (ions) by passing through a thin carbon foil, alignment, orientation, and coherence are produced in their excited levels. The emission lines from these levels are polarized, and in some cases their temporal decay contains modulations which are called quantum beats. The frequencies of these beats correspond to the energy splittings of the upper levels, and the amplitudes and the phases are determined by the details of the state of these atoms (ions). The initial state and its subsequent development are expressed by the density matrix operator and its temporal evolution, respectively. The diagonal element represents the ''population'' of a magnetic sublevel, and the off-diagonal element represents the coherence, or the phase correlation, between a pair of the sublevels. From a measurement of the polarization or of the quantum beats of a line, we can determine the state of the excited atoms at the instance of the light emission. By tracing the temporal development back to the instance of excitation, we may be able to determine the initial state, or the initial density matrix operator. The initial state is the result of the foil excitation, and the matrix elements contain the information concerning the excitation mechanism in the foil-atom interaction.

From now on, we concentrate on the hydrogen $n=2$ atoms which are excited by a foil which is set perpendicular to the beam direction. No orientation is produced in this symmetry. Table I gives the nonvanishing matrix elements on the uncoupled basis. The system evolves and an example of the temporal developments of the Lyman-α line (121.6 nm) intensity subsequent to excitation is shown in Fig. 1(a); this is a calculation result for a particular initial state of excitation. The single exponential decay is superposed by a quantum beat having the frequency corresponding to the $2\,^2P_{3/2}$–$2\,^2P_{1/2}$ splitting (10.97 GHz). Figure 2(a) shows the relative energy values of these levels on the left-hand side ends. The relative amplitude of the quantum beat is a measure of the population imbalance of the sublevels on the uncoupled basis, $(\sigma_{pp1}-\sigma_{pp0})/(\sigma_{pp1}+\sigma_{pp0})$, or the align-

ment. Dobberstein *et al.* [1] determined the initial alignment by observing the quantum beat in the decay curve and their result is given in Fig. 3(g).

When an electric field is present, the $2\,^2S$ level and $2\,^2P$ level mix each other as shown in Fig. 2(b), where the degrees of Stark mixing of the eight pure sublevels $2\,^2L_{j,m_j}^{\text{pure}}$ into the real sublevel ''$2\,^2P_{1/2,1/2}$'' are shown as an example. The Lyman-α line intensity now contains a contribution from the $1\,^2S$–$2\,^2S$ transition. Figure 2(a) shows the energy position of these real levels as a function of the field strength. The temporal decay now has the beat corresponding to the $2\,^2S_{1/2}$–$2\,^2P_{1/2}$ splitting, i.e., the Lamb shift (1.06 GHz in the low field limit), in addition to the beat corresponding to the fine structure splitting. Examples are shown in Fig. 1(b) as the initial decay in the period denoted as ''field region.'' In the electric field, the energy splittings of the levels become larger [Fig. 2(a)], so that the frequencies of the quantum beats become higher as seen in Fig. 1(b). Thus the beats become more difficult to resolve in experiment. In order to resolve them, the observation (slit) width has to be narrower, resulting in lower intensities and thus a low signal-to-noise ratio.

Alguard and Drake [2] observed the quantum beats in the motional electric field perpendicular to both the beam direction and the optical axis for observation [note that in Fig. 1(b) the field is parallel to the beam direction.] By adopting a rather low spatial resolution they observed only the lower frequency beat corresponding to the Stark-shifted Lamb shift splitting. From the relative amplitude they determined the

TABLE I. The nonvanishing matrix elements on the uncoupled basis.

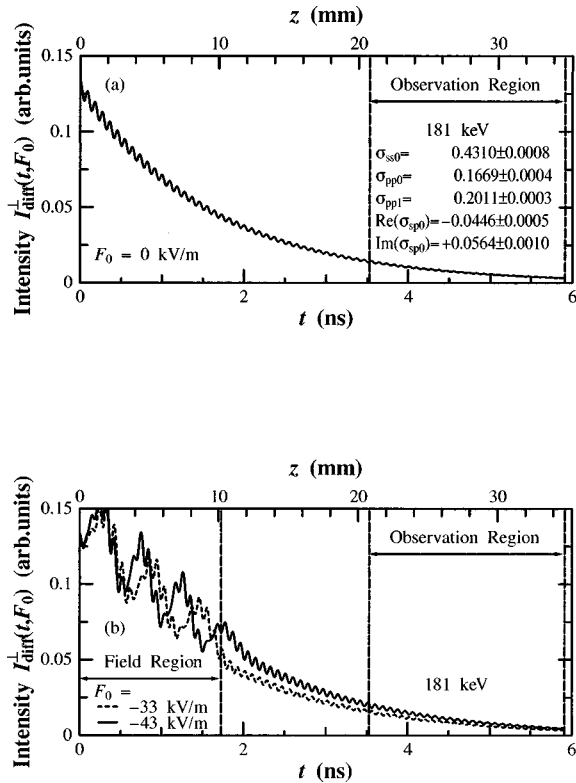|	$|s0\rangle$	$|p1\rangle$	$|p0\rangle$	$|p-1\rangle$
$\langle s0|$	σ_{ss0}		σ_{sp0}	
$\langle p1|$		σ_{pp1}		
$\langle p0|$	σ_{sp0}^*		σ_{pp0}	
$\langle p-1|$				σ_{pp1}

FIG. 1. The calculated intensity $I_{\text{diff}}^{\perp}(t, F_0)$ of the Lyman-α line as a function of time from the excitation. The region for light observation is denoted as ''Observation Region.'' The initial density matrix elements are assumed to be those determined from the measurement shown in Fig. 7. (a) An electric field is absent, (b) an electric field is applied as shown in Fig. 5 with $F_0 = -33$ kV/m (-----), which gives one of the bottoms of the beat in Fig. 7(b), and with $F_0 = -43$ kV/m (———), which gives the adjacent top in Fig. 7(b).

population ratio between the $2S$ and $2P$ levels. The result is given in Fig. 3(f).

The contribution from the coherence between the S and P levels (Table I) to the observed Lyman-α intensity has opposite signs for the opposite directions of the electric field. [See Appendix B and Figs. 6(d) and 6(e).] Eck [3] proposed that the S-P coherence can be determined from a comparison of the two decay curves with the electric field parallel or anti-parallel to the beam direction. Sellin et $al.$ and Gaupp et $al.$ [4,5] applied this method and determined the S-P coherence. In Gaupp et $al.$'s data analysis, previous results of the $2P$ alignment [1] and the ratio of the $2S$ to the $2P$ populations [2] was used. The result is given in Figs. 3(d) and 3(e). Gabrielse [6] determined the ratio of the $2S$ to the $2P$ populations and the coherence for a wide beam energy range (Fig. 3). The previous result of the $2P$ alignment by Winter and Bukow [7] (mentioned later) was used [see Fig. 3(g)]. Their definition of the coherence term, however, is ambiguous so that their result is not shown. These authors [4–6] observed only the lower frequency beat corresponding to the Stark-shifted Lamb shift splitting.

Since the electric field mixes the $2P$ level into the $2S$ level, inducing the $1\,^2S - 2\,^2S$ transition, an increase in intensity against the electric field strength [compare Figs. 1(a) and 1(b)] corresponds to the relative population of $2S$ to $2P$.
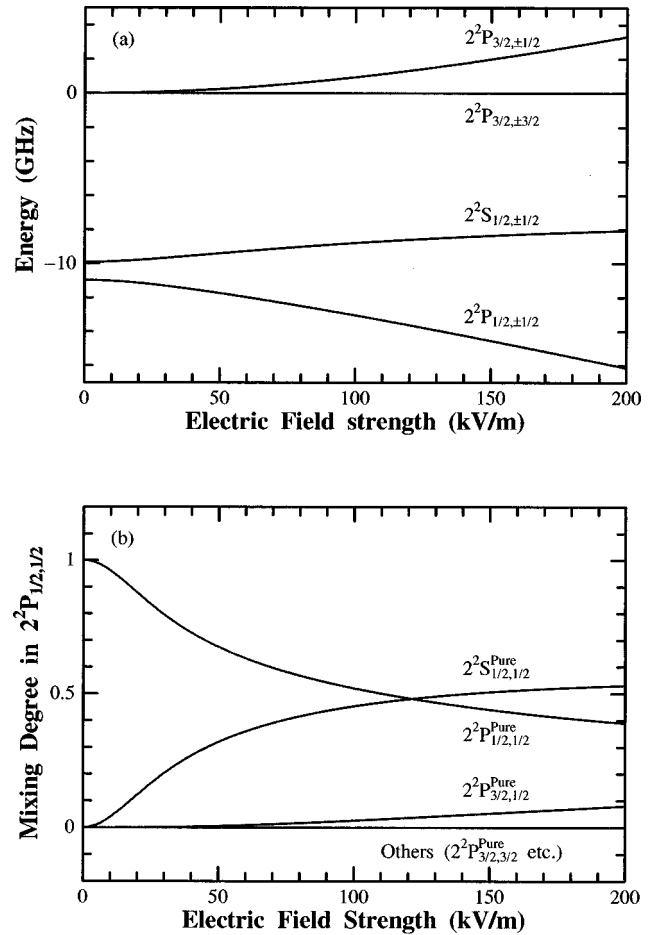

FIG. 2. (a) The relative energy values of the levels of H $(n=2)$ atoms with respect to $2\,^2P_{3/2,\pm 3/2}$ as functions of the electric field strength (it is not F_0 defined later). The $2\,^2P_{3/2} - 2\,^2P_{1/2}$ energy splitting in the low field limit is 10.97 GHz (fine structure) and the $2\,^2S_{1/2} - 2\,^2P_{1/2}$ energy splitting in the low field limit is 1.06 GHz (the Lamb shift). (b) The degree of Stark mixing in the real ''$2\,^2P_{1/2,1/2}$'' sublevel. The four curves represent the mixing degree of each of the eight pure sublevels; $2\,^2P_{1/2,1/2}^{\text{pure}}$, $2\,^2S_{1/2,1/2}^{\text{pure}}$, $2\,^2P_{3/2,1/2}^{\text{pure}}$ and the other five sublevels ($2\,^2P_{3/2,\pm 3/2}^{\text{pure}}$, $2\,^2P_{1/2,-1/2}^{\text{pure}}$, $2\,^2S_{1/2,-1/2}^{\text{pure}}$, $2\,^2P_{3/2,-1/2}^{\text{pure}}$). Since the energy of $2\,^2P_{3/2,1/2}^{\text{pure}}$ is far from that of $2\,^2P_{1/2,1/2}^{\text{pure}}$ as compared with that of $2\,^2S_{1/2,1/2}^{\text{pure}}$, the mixing degree of $2\,^2P_{3/2,1/2}^{\text{pure}}$ is small. Since the field couples sublevels which have the same projection components of j on the field direction, $2\,^2P_{3/2,3/2}^{\text{pure}}$ or $2\,^2P_{3/2,-3/2}^{\text{pure}}$ does not mix with other sublevels.

Clouvas et $al.$ [8] measured the Lyman-α line intensity integrated over a certain time interval in the external field as a function of its strength and direction. They determined the population ratio [Fig. 3(f)], and concluded that the coherence is negligibly small.

All the experiments introduced above were concerned with the line intensity with the polarized components unresolved. Polarization is another source of information concerning the state of atoms. Winter and Bukow [7] measured the polarization of the Lyman-α line and determined the alignment of the $2P$ level for the low energy range where the quantum beat measurement was impractical [Fig. 3(g)].

In principle, from a single measurement of the quantum beats with the polarized components unresolved, the state of the atoms, i.e., all the populations, alignment, and coherence, could be determined. However, the experiments introduced
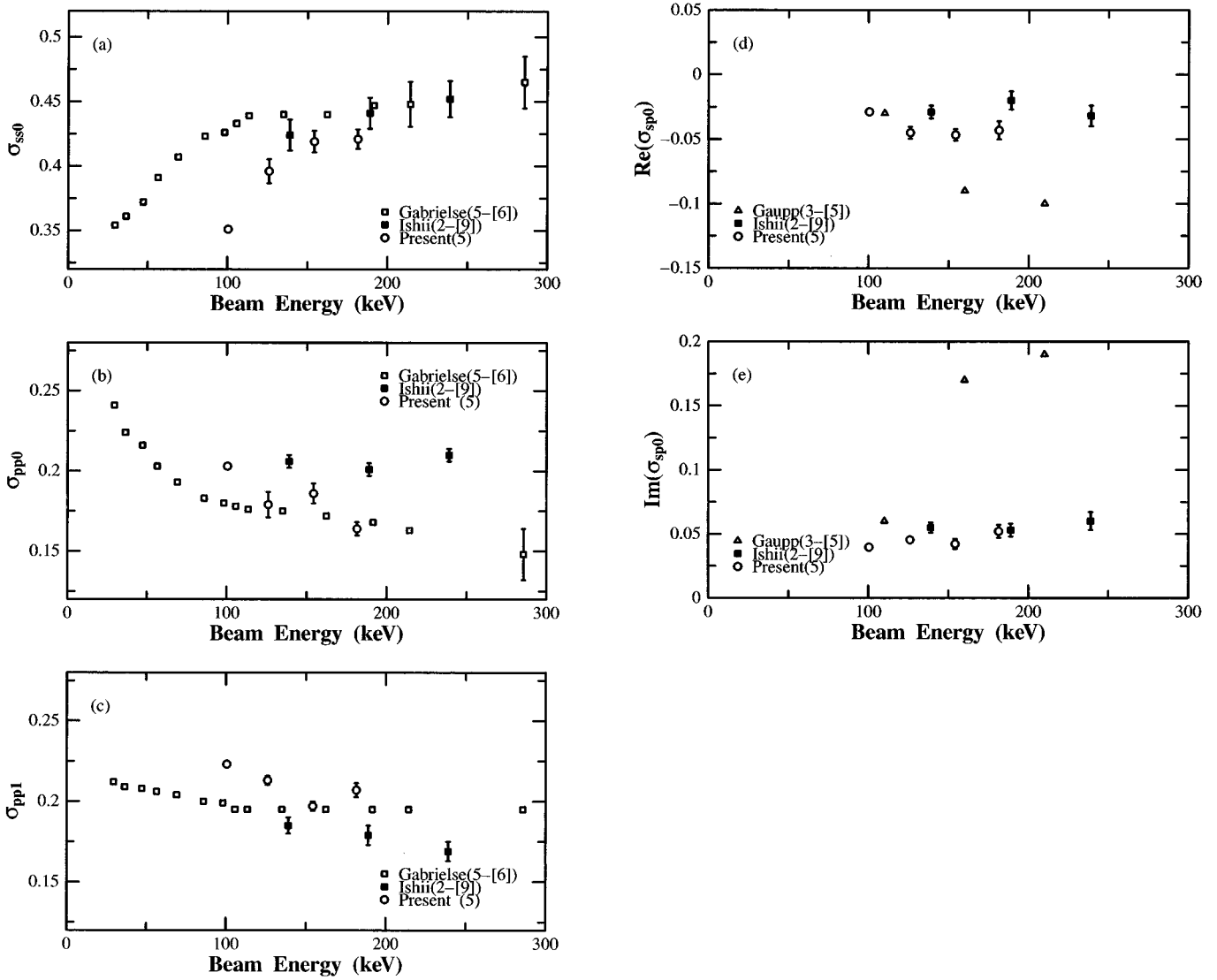
FIG. 3. The initial density matrix elements vs the beam energy. The surface density of the foils used in each experiment is shown in the parentheses in units of $\mu g/cm^2$, with the format of (surface density)-(reference number). (a) σ_{ss0}, (b) σ_{pp0}, (c) σ_{pp1}, (d) $Re(\sigma_{sp0})$, (e) $Im(\sigma_{sp0})$, (f) the ratio of the $2S$ to the $2P$ populations; $\sigma_{ss0}/(\sigma_{pp0}+2\sigma_{pp1})$, (f) the alignment of the $2P$ level; $(\sigma_{pp1}-\sigma_{pp0})/(\sigma_{pp1}+\sigma_{pp0})$.

above [1,2,4–6,8] succeeded in determining only a part of it. It is because, with the polarized components unresolved, (1) as Gabrielse pointed out [6], the magnetic sublevel populations (so the alignment) of the $2P$ level is difficult to determine from the quantum beat measurement, since the patterns of the beat derived from each of them are similar. (2) Since the S-P coherence term (the off-diagonal element) is usually small in comparison with the diagonal elements, the relative amplitude of the beat stemming from the S-P coherence is small. If we incorporate a polarization resolved measurement with a quantum beat measurement, that would help the simultaneous determination of the above quantities. This is because the intensity ratio between the linearly polarized components, or the linear Stokes parameter, depends strongly on the P level alignment.

Ishii *et al.* [9] observed the Lyman-α line in an electric field with a high enough spatial resolution to resolve the fine structure quantum beat and with the polarized components resolved. By adopting a MgF_2 coated toroidal mirror as a

polarizer, they accomplished a high spatial resolution. They succeeded in determining all the nonzero density matrix elements by a single measurement, as shown as "Ishii" in Fig. 3. The results, however, are accompanied by large uncertainties, and, in some case, substantially different from other measurements (negative alignments in contrast to the positive ones by other experiments). It may be concluded that their signal-to-noise ratio (SNR) values were not high enough.

The ideal experiment would be the one in which we apply an electric field and observe the quantum beats with the polarized components resolved, still with a high enough SNR value. For the last requirement we should take the observation region wide as shown in Fig. 1. Figure 1(b) suggests that, if we apply an electric field over a certain period and turn it off, the behavior of the subsequent decay curve is strongly dependent on the beat structure during the field region. This can be understood from Fig. 2: Suppose the electric field starts from null, increases to a certain value, and
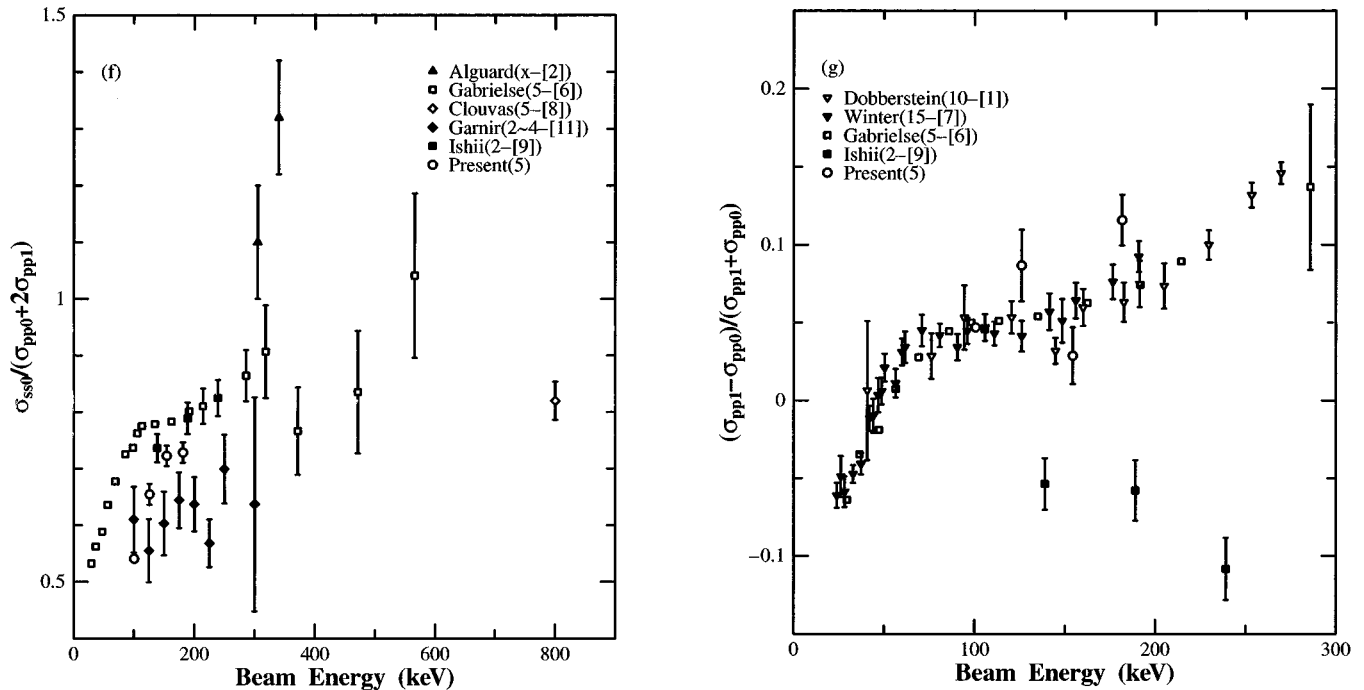
FIG. 3. *(Continued)*.

then decreases to null. The atom starts from its initial state and experiences phase changes according to the changes in energy and level mixing in the field. When it returns to the null field, the initial atomic state has been modified, and this state serves as the initial states of the subsequent decay of the Lyman-α line intensity.

Thus the following geometry may fulfill all the requirements: Just after the foil excitation an electric field is applied over a certain distance and after that we observe the fluorescence over a certain distance with the polarized component resolved. On the basis of this consideration we developed a technique in which, by measuring the line intensity with a high SNR, we can determine all the matrix elements in a single experiment. In the following we describe the method and the result.

II. EXPERIMENTAL SETUP

A proton (H^+) beam was produced by an electrostatic accelerator and led to a collision chamber. Figure 4 shows schematically the structure inside the chamber: a target foil, and a set of electrode disks. The pressure is about 5×10^{-7} torr. The observation region of the beam is inside the electrode tube. The part of the structure from the electrode disk I to the electrode disk II is surrounded by a grounded cell (200 mm$\times$150 mm$\times$160 mm, not shown in Fig. 4) made of Permalloy which has an entrance hole (8.0 mm diameter), an exit hole (10.0 mm diameter), and an opening (75 mm$\times$15 mm) for light observation. The purpose of this cell is to shield the magnetic and electric fields outside. The earth magnetic field inside is estimated to be
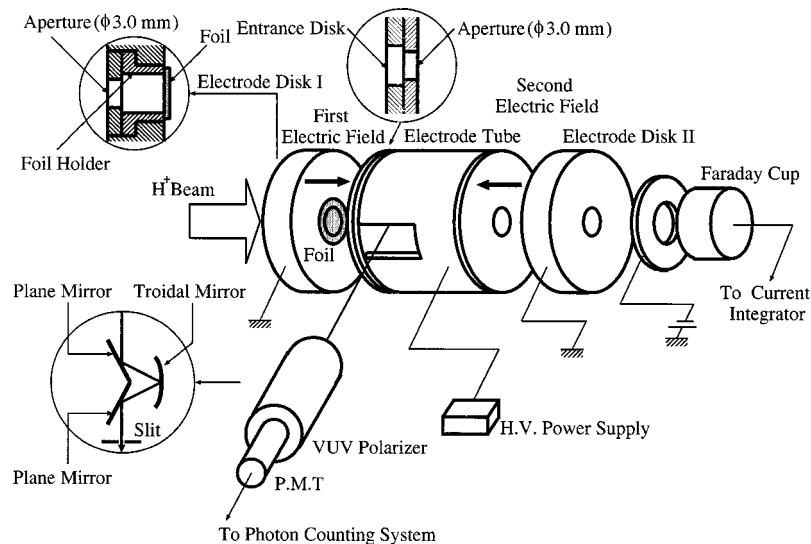

FIG. 4. The experimental setup. Insets show the detailed structure of the electrode disk I, the entrance side of the electrode tube, and the vuv polarizer.
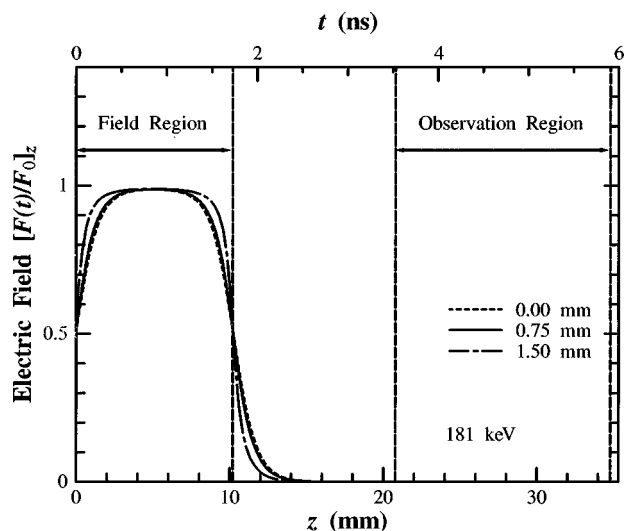
FIG. 5. The z component of the electric field in the region of the electrode disk I and the electrode tube, $[F(t)/F_0]_z$, where F_0 is the voltage supplied to the electrode tube divided by 10.2 mm with the sign reversed. The upper abscissa is the time scale for hydrogen atoms with 181 keV. The three curves give $[F(t)/F_0]_z$ on the center axis, at 0.75 mm from it and at 1.5 mm, respectively.

less than 0.01 G. Therefore, in our experiment, the motional electric field is less than 5 V/m for hydrogen atoms moving with the energy of 180 keV and is well neglected.

An aperture in front of the foil limits the beam diameter hitting the target foil to 3.0 mm. A carbon foil of surface density of 5 μg/cm^2 (YISSUM Research Development Company) was used. The foil is self-supported on an aluminum holder with a center hole (diameter 4.0 mm), which is inserted in the center hole of the grounded cylindrical aluminum electrode disk I (diameter 120.0 mm, thickness 20.0 mm). The foil is on the same plane as the downstream side surface of the electrode disk I.

The cylindrical aluminum electrode tube is placed 10.2 mm downstream from the electrode disk I. A Teflon cylindrical spacer (10.2 mm thickness, not shown in Fig. 4) with a center hole is inserted between them, in order to set the distance between the downstream surface of the disk I and the upstream surface of the electrode tube with high accuracy, and to prevent the stray light from coming out. The electrode tube (diameter 120.0 mm, total length 71.1 mm, thickness 10.0 mm) has an aluminum entrance disk (diameter 120.0 mm, thickness 5.0 mm) which has a center hole (diameter 4.0 mm) and an aperture (diameter 3.0 mm). This tube has an opening (20.0 mm×12.0 mm) on the side wall for light observation. An aluminum exit disk (diameter 120.0 mm, thickness 3.5 mm) with a center hole (diameter 4.0 mm) is placed at the end of the tube. The electrode tube was held at a potential of $-2000-+2000$ V by a high voltage power supply (ORTEC 556), which was controlled by a personal computer. The supplied voltage was monitored by a digital voltmeter. Thus an electric field (the first electric field) was created between the electrode disk I and the electrode tube.

The electric field in the space around the electrode disk I and the electrode tube was calculated numerically by the finite element method (FEM). Figure 5 shows the z (the direction of the beam) component of the electric field calculated: $[F(t)/F_0]_z$, where F_0 is the voltage supplied to the

electrode tube divided by 10.2 mm with the sign reversed. The upper abscissa is the time scale for hydrogen atoms with the energy of 181 keV. For convenience of the later calculation, the field $F(t)$ is treated as a function of time t. In addition to the t (or z) dependence, the field $F(t)$ depends on the radial position. The three curves give $[F(t)/F_0]_z$ on the center axis, at 0.75 mm from it and at 1.5 mm (beam edge), respectively. In the following, in order to represent the entire field $F(t)$ in these regions and to denote its dependence on the voltage supplied to the tube, F_0 is used and called "*field strength*" which takes both positive and negative values.

Further downstream a grounded cylindrical aluminum electrode disk II (diameter 120.0 mm, thickness 20.0 mm) with a center hole (diameter 4.0 mm), is placed symmetrically to the disk I. The electric field between this disk and the tube (the second electric field) is necessary in order to repel the convoy electrons, when the electrode tube is held at a positive potential.

After passage of the beam through the carbon foil, a part ($\sim 10\%$) of the ions was neutralized and the rest remained to be ions. The beam which passed through the set of electrode disks was collected by a Faraday cup far downstream. The beam current due to the ions was integrated, digitized (ORTEC 439) with 10^2 pulse/μC, counted, and finally transferred to a personal computer. The bottom of the Faraday cup has an opening which is covered with a tungsten mesh. A part of the beam passing through the mesh hit the quartz window. The light from the fused quartz surface showed the beam shape and was utilized for the purpose of checking of the foil breakage. The electrode biased to -200 V to the ground potential having aperture of 27 mm diameter was placed in front of the Faraday cup. This electrode prevented electrons from coming into the cup and also the secondary electrons produced inside the cup going out. Owing to the grounded cell, this electric potential did not affect the atoms inside it.

The light emitted by the beam atoms went through the openings of the electrode tube and the cell, in the direction perpendicular to the beam direction. The solid angle of 2.4×10^{-3} sr was determined by the vacuum ultraviolet (vuv) polarizer (Fig. 4). The polarizer consists of three mirrors. The first mirror is a plane mirror (45 mm×40 mm, thickness 8 mm) of fused silica. The incidence angle is 60°. The second mirror is a toroidal mirror of gold (52 mm×52 mm), with the incidence angle of 30°. The radius of the surface in the plane of incidence is 281.0 mm and that perpendicular to it is 210.0 mm. The third mirror is the same as the first one. By the toroidal mirror, the image of the beam is focused on the aperture (diameter 14.0 mm) in front of the photomultiplier tube (PMT) by one-to-one imaging (focal length 281.0 mm). The optical axis of the incident light on the first mirror and that of the reflected light by the third mirror are on the same straight line. The transmission axis is selected by rotation of these three mirrors around the optical axis. The polarization efficiency is calculated to be 380 according to the conventional optical constants. The efficiency was determined to be 27 in this experiment (see later).

The observation region determined by the aperture in front of the PMT was the part of the beam from 20.8 mm to 34.8 mm downstream from the foil. As is seen in Fig. 1 or

Fig. 5, for example, it spans from 3.53 ns to 5.91 ns in the time scale for 181 keV atoms. It may be noted that the observed integrated intensity is rather insensitive to the exact definition of the observation region. The PMT (HAMAMATSU R1459) has a MgF_2 window which transmits the light with wavelength 120 nm or longer, and has a CsI photocathode (diameter 25.0 mm) which is sensitive to light below 200 nm. The only emission line from hydrogen atoms in this wavelength range is the Lyman-α line. The output signal from the PMT was counted by the standard photon counting technique, and transferred to the personal computer.

III. PRINCIPLE OF EXPERIMENT AND ANALYSIS METHOD

The quantization axis is chosen to be the beam direction ($+z$ direction). It is assumed that, in passage of an atom through a carbon foil, the interaction affects only the orbital angular momentum and leaves the spin isotropic. The ensemble of excited atoms just after the passage is represented in terms of the uncoupled basis sets $|lm_l\rangle|sm_s\rangle$. Since the foil normal is parallel to the quantization axis, the ensemble is reflection and axially symmetric. The initial density matrix elements in the uncoupled basis set, $\langle l'm_l'sm_s'|\rho(0)|lm_lsm_s\rangle$, satisfy the following relation (see also Table I):

$$\langle l'm_l'sm_s'|\rho(0)|lm_lsm_s\rangle = \sigma_{l'l}|m_l|\delta_{m_lm_l'}\delta_{m_sm_s'}. \quad (1)$$

It is noted that they do not depend on the sign of m_l.

Owing to the spin-orbit interaction, the density matrix operator $\rho(t,F_0)$ is described in terms of the coupled basis $|(ls)jm_j\rangle$. The hyperfine structure is ignored. The time evolution of the density matrix operator satisfies the equation

$$i\hbar\frac{\partial\rho(t,F_0)}{\partial t} = H(t,F_0)\rho(t,F_0) - \rho(t,F_0)H(t,F_0)^\dagger, \quad (2)$$

where $H(t,F_0)$ is the total Hamiltonian of the hydrogen atom and has the form

$$H(t,F_0) = H_0 + H_D + H_F(t,F_0). \quad (3)$$

The first term H_0 consists of the kinetic energy, the electrostatic potential energy, the spin-orbit interaction, and the Lamb shift. The second term H_D is the decay Hamiltonian. The third term $H_F(t,F_0)$ represents the interaction of the atom with the external electric field, given by

$$H_F(t,F_0) = -\boldsymbol{d}\cdot\boldsymbol{F}(t) = +e\boldsymbol{r}\cdot\boldsymbol{F}(t), \quad (4)$$

where $\boldsymbol{d}$ is the electric dipole operator, $\boldsymbol{F}(t)$ is the electric field affecting the atom (shown in Fig. 5), $e(>0)$ is the elementary electric charge, and $\boldsymbol{r}$ is the electron position vector.

For a 181 keV hydrogen atom, for example, maximum rate of the change in the field strength is 200 kV/m per 0.5 ns. If we take the pair of the levels in Fig. 2 that tend to the $2\,^2S_{1/2}$ and $2\,^2P_{1/2}$ in the absence of the field, the "transition" rate $\langle 2\,^2S_{1/2,1/2}|\partial/\partial t|2\,^2P_{1/2,1/2}\rangle$ is estimated from Fig. 2(b) to be $\simeq 10^9$ (s^{-1}) at about 200 kV/m. This is much smaller than the energy difference in the angular frequency

units, $\sim 2\pi\times 5\times 10^9$ (s^{-1}). Thus the evolution is adiabatic throughout the course of time.

The time evolution of the density matrix operator [Eq. (2)] is solved numerically by the Runge-Kutta-Gill method by using the time evolution operator $U(t,F_0)$. The calculation is executed throughout the time from the foil to the end of the observation region with the time step of 0.0024 ns. In the calculation, owing to the limitation of the CPU time, the field on the radial position of 0.75 mm (solid line in Fig. 5) was used as $\boldsymbol{F}(t)$ for all the atoms in the beam and the radial component (14% of F_0 at most) was ignored.

The intensity of the polarized component P of the emission line at time t, $I_{\text{diff}}^P(t,F_0)$, is given by

$$I_{\text{diff}}^P(t,F_0) = \text{tr}[M^P\rho(t,F_0)], \quad (5)$$

where M^P is the monitoring operator which depends on the observation direction and the polarization state P. In the following, $\parallel$ denotes the parallel direction of the linear polarization to the beam, and $\perp$ the perpendicular direction. Details of M^P and the calculation procedure of the intensity are given in Appendix A and B, respectively.

From Eq. (B9), we calculate the intensity. Figure 1 shows an example of $I_{\text{diff}}^\perp(t,F_0)$ calculated for a particular set of the initial density matrix elements. During $t=0-1.73$ ns, the 181 keV atoms pass through the field region between the electrode disk I and the electrode tube, and during $t=3.53-5.91$ ns they are in the observation region. Figure 1(b) is for the cases of $F_0 = -33$ kV/m (the broken curve) and $F_0 = -43$ kV/m (the solid curve).

The intensity of the line in the free space integrated over a time period, say t_0 to t_1, $I_{t_0,t_1}^P(F_0)$, is given by

$$I_{t_0,t_1}^P(F_0) = \int_{t_0}^{t_1} I_{\text{diff}}^P(t,F_0)dt. \quad (6)$$

As is suggested by Fig. 1(b), this integrated intensity has a significant dependence on the field strength. The nonzero matrix elements in Table I gives rise to the intensity (the details of derivation are given in Appendix B)

$$I_{t_0,t_1}^P(F_0) = \sigma_{ss0}I_{ss0;t_0,t_1}^P(F_0) + \sigma_{pp0}I_{pp0;t_0,t_1}^P(F_0)$$
$$+ \sigma_{pp1}I_{pp1;t_0,t_1}^P(F_0) + \text{Re}(\sigma_{sp0})I_{\text{Re}(sp0);t_0,t_1}^P(F_0)$$
$$+ \text{Im}(\sigma_{sp0})I_{\text{Im}(sp0);t_0,t_1}^P(F_0), \quad (7)$$

where $\text{Re}(\sigma_{sp0})$ represents the real part of the off-diagonal element σ_{sp0} and $\text{Im}(\sigma_{sp0})$ its imaginary part. We call $I_{l,l',m_l;t_0,t_1}^P(F_0)$ the fundamental intensity. It is calculated from M^P,t_0,t_1, the field $\boldsymbol{F}(t)$, and known parameters such as the energy values, the A coefficients and the wave functions. Since the field $\boldsymbol{F}(t)$ is calculated numerically, the fundamental intensity $I_{l,l',m_l;t_0,t_1}^P(F_0)$ is calculated numerically, and an example is shown in Fig. 6.

Roughly speaking, the fundamental intensity $I_{ss0;t_0,t_1}^P(F_0)$ as a function of F_0 increases against $|F_0|$ [Fig. 6(a)]. This is, of course, due to the mixing of the P levels in the S level [Fig. 2(b)]. Thus the symmetric increase in the signal gives the relative population σ_{ss0}. The populations σ_{pp0}
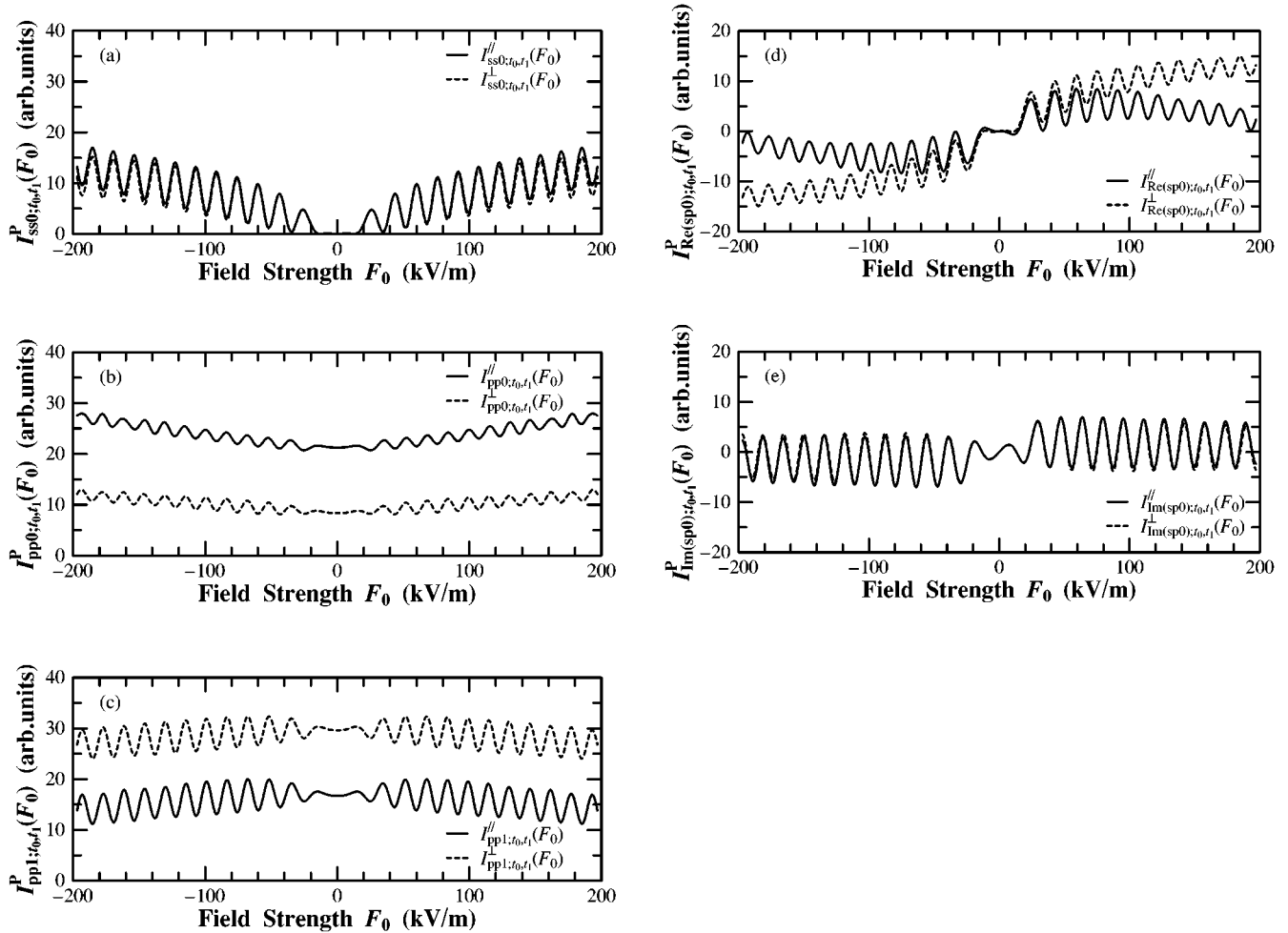
FIG. 6. The fundamental intensities for 181 keV. (a) $I_{ss0,t_0,t_1}^{\parallel}(F_0)$ (———) or $I_{ss0,t_0,t_1}^{\perp}(F_0)$ (-----). (b) $I_{pp0,t_0,t_1}^{\parallel}(F_0)$ (———) or $I_{pp0,t_0,t_1}^{\perp}(F_0)$ (-----). (c) $I_{pp1,t_0,t_1}^{\parallel}(F_0)$ (———) or $I_{pp1,t_0,t_1}^{\perp}(F_0)$ (-----). (d) $I_{\mathrm{Re}(sp0),t_0,t_1}^{\parallel}(F_0)$ (———) or $I_{\mathrm{Re}(sp0),t_0,t_1}^{\perp}(F_0)$ (-----). (e) $I_{\mathrm{Im}(sp0),t_0,t_1}^{\parallel}(F_0)$ (———) or $I_{\mathrm{Im}(sp0),t_0,t_1}^{\perp}(F_0)$ (-----).

and σ_{pp1} give the opposite intensity ratios of the polarized components [Figs. 6(b) and 6(c)]. The ratio $I_{t_0,t_1}^{\parallel}(F_0)/I_{t_0,t_1}^{\perp}(F_0)$ results in the alignment, or $\sigma_{pp0}/\sigma_{pp1}$. The coherence gives the asymmetry of intensity for the sign of F_0 [Figs. 6(d) and 6(e)]. It is noted that the beats of the fundamental intensities $I_{ss0;t_0,t_1}^{P}(F_0)$, $I_{pp0;t_0,t_1}^{P}(F_0)$, $I_{pp1;t_0,t_1}^{P}(F_0)$, and $I_{\mathrm{Re}(sp0);t_0,t_1}^{P}(F_0)$ have a common phase; i.e. in phase or antiphase. The fundamental intensity for the imaginary part of the coherence has the beat out of phase by $\pi/2$ or $3\pi/2$ from the other beats [Fig. 6(e)]. Thus the phase of the signal gives this quantity. The period of the beat gives a very good measure of the speed of the atoms.

The curves in Fig. 7 correspond to a combination of the fundamental intensities for the particular set of the initial density matrix elements as mentioned in Fig. 1(a). We call these modulations the "field-dependent quantum beats". The F_0 value of -43 kV/m in Fig. 1(b) gives one of the tops of the modulation of the curve in Fig. 7(b) and -33 kV/m gives one of the bottoms. Thus, in our method, even if the observation region is significantly wider than the periods of the original quantum beats, significant modulations of intensity is retrieved. This is contrasted to the experiment by Clouvas et al. [8], in which a line intensity is observed with

a wide observation width in a field region and the modulations are smeared out [compare $I_{\mathrm{diff}}^{\perp}(t,F_0)$'s before and after $t=1.73$ ns in Fig. 1(b)].

IV. EXPERIMENTAL PROCEDURE AND RESULTS

A systematic procedure was adopted for measuring the intensity of the linearly polarized components of the Lyman-α line as a function of the external electric field strength and direction. First, by holding the center electrode tube at a positive potential with respect to the ground (created field direction is denoted by "neg."), the transmission axis of the vuv polarizer was set parallel ($\parallel$) to the beam direction. The absolute value of the center electrode tube potential was increased from 0 to 2000 V with 20 V steps. At each step, the number of photoelectron pulses was counted for 5 s, simultaneously with the measurement of the beam current with the Faraday cup. If the beam current deviated by more than $\pm10\%$ from a preset value, the ion beam current was adjusted and then the procedure was repeated. For another 5 s, the number of photoelectron pulses was counted. The observed intensity $I_O^{\parallel}(F_0)$ [and $I_O^{\perp}(F_0)$] was defined as the sum of the photon counts divided by the collected ion charge (typically 15 μC) during the measurement unit (10 s).
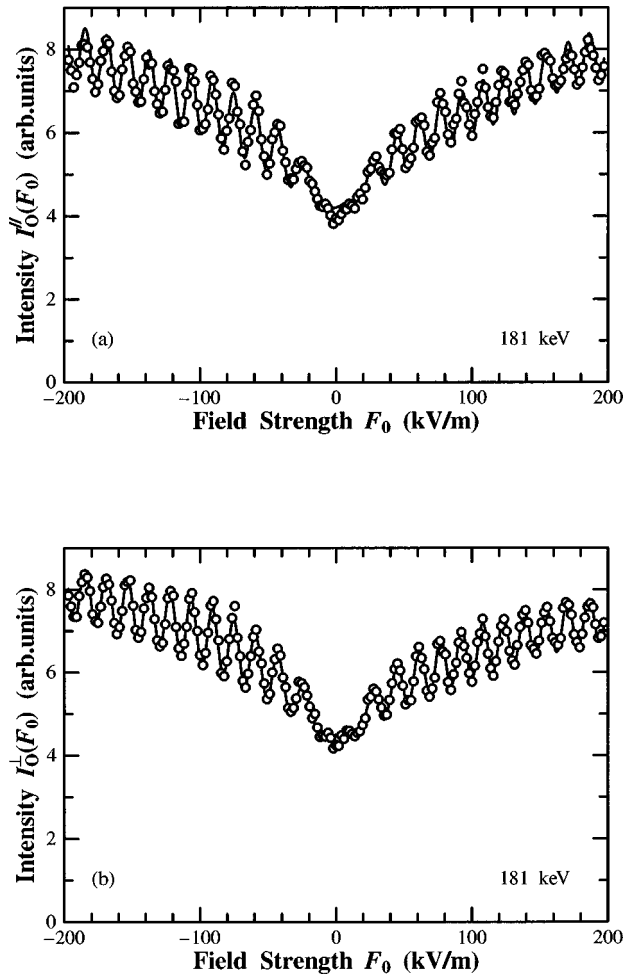
FIG. 7. An example of the observed Lyman-α intensities. The abscissa is the field strength F_0. The beam energy is 181 keV. The curve is the result of the least squares fitting to Eq. (7). (a) $I_O^{\parallel}(F_0)$ and (b) $I_O^{\perp}(F_0)$.

After completion of this procedure the potential of the electrode tube was switched to negative (pos.), and a similar procedure was followed. Then, the transmission axis of the vuv polarizer was rotated by 90° ($\perp$). Thus one complete series (one single measurement) consisted of neg./$\parallel$→pos./$\parallel$→pos./$\perp$→neg./$\perp$ (series A). The next series consisted of →neg./$\perp$→pos./$\perp$→pos./$\parallel$→neg./$\parallel$ (series B). Then a similar procedure was followed. A total of four single measurements were executed for one beam energy.

An example of the observed intensities as a function of F_0 by *one* single measurement is shown in Fig. 7: (a) shows $I_O^{\parallel}(F_0)$ and (b) shows $I_O^{\perp}(F_0)$. The $I_O^{\parallel}(F_0)$ and $I_O^{\perp}(F_0)$ were least squares fitted by Eq. (7), i.e., by linear combinations of

$I_{t_0,t_1}^{\parallel}(F_0)$ and $I_{t_0,t_1}^{\perp}(F_0)$. Here, the initial matrix elements (Table I), which were so normalized that their trace was 1 (the number of independent parameters were 4), the polarization efficiency of the vuv polarizer, the detection efficiency of the PMT and the atom energy, were adjusted and determined. The curves in this figure are the result of the fitting. The matrix elements and the beam energy given in Fig. 1(a) were obtained by this single measurement shown in Fig. 7. Their uncertainties come from the statistical ones.

All the initial density matrix elements had no dependence on the order of measurement (series A or B). Among the matrix elements obtained by each of the four single measurements, only σ_{ss0} showed a slight dependence on the ion beam dose to the foil [10] at all the beam energies; the population of the 2s level (σ_{ss0}) increased with the beam dose by several percent. The magnitude was larger for the lower beam energy.

We averaged the matrix elements determined in each of the four measurements and obtained the result shown in Table II. The uncertainty represents PE (0.6745 times standard deviation of the four values). It may be noted that these uncertainties are larger than those in Fig. 1(a) by an order of magnitude. The beam dose effect may contribute to the large uncertainties. For 100 keV, only two data were taken and the uncertainty was not determined.

Figure 3 compares the present result with the previous ones [1,2,5–9,11]. The surface density of the foil used in each experiment is also shown in the parentheses in units of μg/cm^2 with the format of (surface density)-(reference number). It is not clear whether the energy in the literature represents the incident ion energy or outgoing atom energy. In view of the difficulties in the previous experiments, as has been mentioned in the Introduction, and the differences in the surface densities of the foil, the overall agreement should be regarded good, except for a few cases. These cases are (i) the σ_{ss0} by Gabrielse [6], (ii) the σ_{sp0} by Gaupp *et al.* [5], (iii) the population ratio between 2S and 2P by Alguard and Drake [2], and (iv) the alignment by Ishii *et al.* [9]. In the last case of alignment our result shows the local minimum at 154 keV. This may be in accordance with the result by Dobberstein *et al.* [1]. The differences of (i) and (iii) may be attributed to the beam dose effects which is intense for lower beam energy.

V. DISCUSSION

According to Burgdörfer's semiclassical interpretation [12], the real part of the off-diagonal element Re(σ_{sp0}) represents the ensemble mean of the z component of the electric dipole; $\langle d_z \rangle$, and the imaginary part Im(σ_{sp0}) the mean of the z component of the velocity of the electron at the perihelion of the elliptic orbit; $\langle [L \times A]_z \rangle$. Here, L is the angular mo-

TABLE II. Obtained initial density matrix elements. The uncertainty represents the PE (where PE denotes probable error).

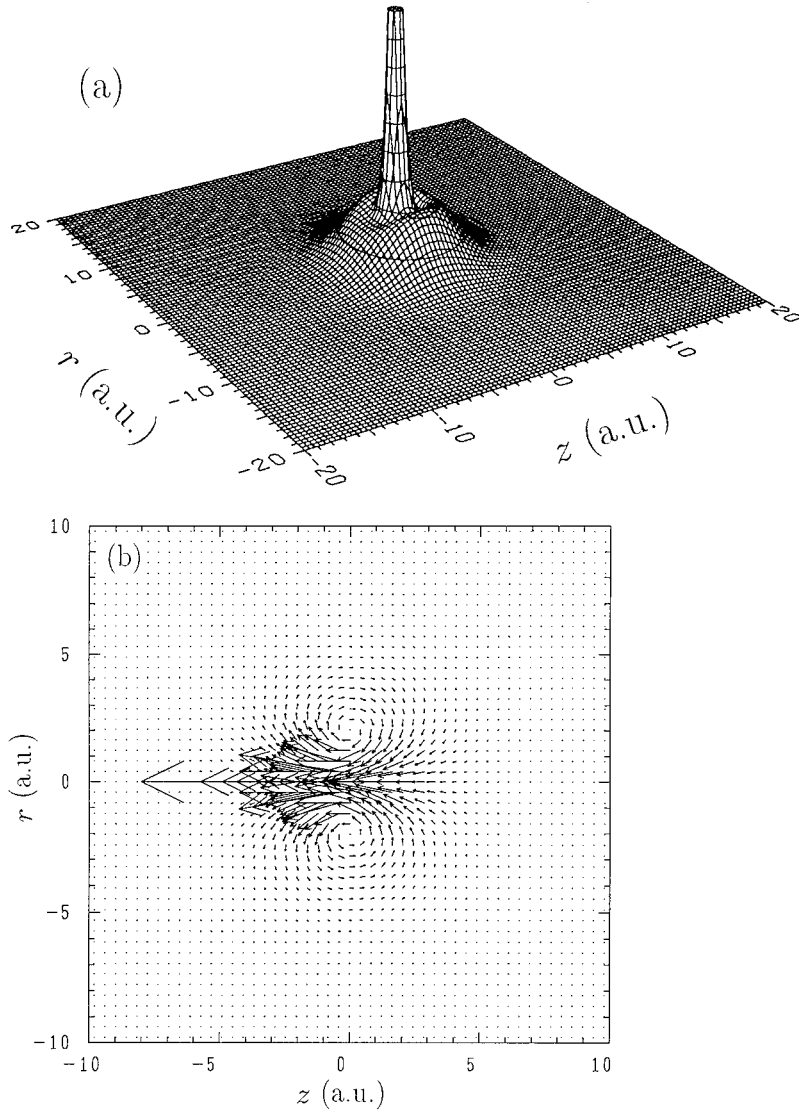| Energy	σ_{ss0}	σ_{pp0}	σ_{pp1}	Re(σ_{sp0})	Im(σ_{sp0})
100.5	0.351	0.203	0.223	-0.029	$+0.040$
126.0±0.8	0.396±0.009	0.179±0.008	0.213±0.003	-0.045±0.005	$+0.045$±0.002
154.3±0.3	0.419±0.008	0.186±0.006	0.197±0.003	-0.047±0.004	$+0.042$±0.004
181.5±0.7	0.421±0.008	0.164±0.004	0.207±0.004	-0.043±0.007	$+0.052$±0.005

FIG. 8. (a) The electron probability density $D(r)$ for 181.5 keV H ($n=2$) atoms. The hydrogen atoms travel in the positive direction of the z axis. The direction perpendicular to it is the arbitrary radial direction (r). The range shown is $-20a_0 \leqslant z \leqslant +20a_0$ and $-20a_0 \leqslant r \leqslant +20a_0$, where a_0 is the Bohr radius. (b) The electron probability current density $j(r)$. The arrows represent $j(r)$. The range shown is $-10a_0 \leqslant z \leqslant +10a_0$ and $-10a_0 \leqslant r \leqslant +10a_0$.

mentum operator, and A is the Runge-Lenz operator. The present experiment shows that, in the energy range 100–180 keV, the electron cloud of the H($n=2$) atom just after the excitation extends to be in the forward direction from the proton, and the mean of the z component of the velocity of the electron at the perihelion is negative.

According to Havener *et al.*'s quantum mechanical interpretation [13], the electron probability density $D(r)$ and the electron probability current density $j(r)$ are given by the diagonal and off-diagonal elements. Figure 8(a) shows $D(r)$ derived from the density matrix elements listed in Table II for 181.5 keV H($n=2$) atoms. The hydrogen atoms travel in the positive direction of the z axis. The direction perpendicular to it is the arbitrary radial direction (r). This figure shows that the electron probability density is higher in the forward direction to the proton than backward. It is due to the negative Re(σ_{sp0}). Figure 8(b) shows $j(r)$. The flow direction of the $j(r)$ is determined by Im(σ_{sp0}).

In Fig. 7, in the range of the field -10–$+10$ kV/m, the observed intensities of both the polarized components are slightly lower than the fitted curves. This may be related with the cascade contribution from the $3S$ level: for higher field the cascade enhances the observed intensity slightly owing to the Stark mixing between the pure $3S$ and $3P$, $3D$ levels.

The cascade contributions from the pure $3P$ and $3D$ levels are almost independent of the field strength.

ACKNOWLEDGMENTS

APPENDIX A: MONITORING OPERATOR

The monitoring operator M^P is defined by

$$M^P = K^P(\lambda) \sum_0 (\boldsymbol{\epsilon} \cdot \boldsymbol{d})^{\dagger} |0\rangle\langle 0| (\boldsymbol{\epsilon} \cdot \boldsymbol{d}), \qquad \text{(A1)}$$

where $K^P(\lambda)$ is a constant which contains the solid angle of the optics, the efficiency of the PMT and so on, $\boldsymbol{\epsilon}$ is the polarization vector which specifies the observed polarization

state, and $\boldsymbol{d}$ is the electric dipole operator. The ket $|0\rangle$ represents the lower states of the transition.

APPENDIX B: FUNDAMENTAL INTENSITY

The state vectors on the uncoupled basis sets are represented by $|a\rangle, |b\rangle, \ldots$ and those on the coupled basis sets are represented by $|\alpha\rangle, |\beta\rangle, \ldots$. Namely, the following simplified symbols are used:

$$|a\rangle = |l_a, m_{l_a}, s_a, m_{s_a}\rangle, \tag{B1}$$

$$|\alpha\rangle = |j_\alpha, m_{j_\alpha}\rangle. \tag{B2}$$

With the time evolution operator $U(t)$ [14], the density matrix operator at time t is given by

$$\rho(t,F_0) = U(t,F_0)\rho(0)U(t,F_0)^\dagger. \tag{B3}$$

From Eq. (B3) and Eq. (2), the time evolution operator $U(t,F_0)$ satisfies the following differential equation:

$$i\hbar \frac{\partial U(t,F_0)}{\partial t} = H(t,F_0)U(t,F_0), \tag{B4}$$

where $H(t,F_0)$ is the total Hamiltonian of the ensemble given by Eq. (3). In this work, Eq. (B4) is solved numerically by the Runge-Kutta-Gill method.

The polarized component intensity of the line at time t, $I_{\text{diff}}^P(t,F_0)$, is obtained from $\rho(t,F_0)$ by Eq. (5).

$$I_{\text{diff}}^P(t,F_0) = \text{tr}[M^P \rho(t,F_0)] \tag{B5}$$

$$= \sum_\alpha \sum_\beta \langle \alpha | M^P | \beta \rangle \langle \beta | \rho(t,F_0) | \alpha \rangle \tag{B6}$$

$$= \sum_\alpha \sum_\beta \langle \alpha | M^P | \beta \rangle \langle \beta | U(t,F_0)\rho(0)U^\dagger(t,F_0) | \alpha \rangle \tag{B7}$$

$$= \sum_\alpha \sum_\beta \sum_\gamma \sum_\delta \langle \alpha | M^P | \beta \rangle \langle \beta | U(t,F_0) | \gamma \rangle \langle \gamma | \rho(0) | \delta \rangle \langle \delta | U^\dagger(t,F_0) | \alpha \rangle \tag{B8}$$

$$= \sum_{j_\alpha, m_{j_\alpha}} \sum_{j_\beta, m_{j_\beta}} \sum_{j_\gamma, m_{j_\gamma}} \sum_{j_\delta, m_{j_\delta}} \sum_{l_\alpha, m_{l_\alpha}, s_\alpha, m_{s_\alpha}} \sum_{l_b, m_{l_b}, s_b, m_{s_b}} \langle j_\alpha, m_{j_\alpha} | M^P | j_\beta, m_{j_\beta} \rangle \langle j_\beta, m_{j_\beta} | U(t,F_0) | j_\gamma, m_{j_\gamma} \rangle$$

$$\times \langle j_\delta, m_{j_\alpha} | U^\dagger(t,F_0) | j_\alpha, m_{j_\alpha} \rangle \langle j_\gamma, m_{j_\gamma} | l_a, m_{l_a}, s_a, m_{s_a} \rangle$$

$$\times \langle l_b, m_{l_b}, s_b, m_{s_b} | j_\delta, m_{j_\delta} \rangle \langle l_a, m_{l_a}, s_a, m_{s_a} | \rho(0) | l_b, m_{l_b}, s_b, m_{s_b} \rangle. \tag{B9}$$

The intensity integrated over time t_0 to t_1, $I_{t_0,t_1}^P(F_0)$, is given by

$$I_{t_0,t_1}^P(F_0) = \int_{t_0}^{t_1} I_{\text{diff}}^P(t,F_0)dt \tag{B10}$$

$$= \sum_{l_a, m_{l_a}, s_a, m_{s_a}} \sum_{l_b, m_{l_b}, s_b, m_{s_b}} \langle l_a, m_{l_a}, s_a, m_{s_a} | \rho(0) | l_b, m_{l_b}, s_b, m_{s_b} \rangle I_{l_a, m_{l_a}, s_a, m_{s_a}, l_b, m_{l_b}, s_b, m_{s_b}; t_0, t_1}^P(F_0), \tag{B11}$$

where, the fundamental intensity $I_{l_a, m_{l_a}, s_a, m_{s_a}, l_b, m_{l_b}, s_b, m_{s_b}; t_0, t_1}^P(F_0)$ is defined by

$$I_{l_a, m_{l_a}, s_a, m_{s_a}, l_b, m_{l_b}, s_b, m_{s_b}; t_0, t_1}^P(F_0) = \int_{t_0}^{t_1} \sum_{j_\alpha, m_{j_\alpha}} \sum_{j_\beta, m_{j_\beta}} \sum_{j_\gamma, m_{j_\gamma}} \sum_{j_\delta, m_{j_\delta}} \langle j_\alpha, m_{j_\alpha} | M^P | j_\beta, m_{j_\beta} \rangle \langle j_\beta, m_{j_\beta} | U(t,F_0) | j_\gamma, m_{j_\gamma} \rangle$$

$$\times \langle j_\delta, m_{j_\delta} | U^\dagger(t,F_0) | j_\alpha, m_{j_\alpha} \rangle \langle j_\gamma, m_{j_\gamma} | l_a, m_{l_a}, s_a, m_{s_a} \rangle \langle l_b, m_{l_b}, s_b, m_{s_b} | j_\delta, m_{j_\delta} \rangle dt. \tag{B12}$$

As has been shown in Table I, the independent nonzero matrix elements are σ_{ss0}, σ_{pp0}, σ_{pp1}, and σ_{sp0}. The diagonal elements are real and the off-diagonal element is complex. The number of unknown parameters to be determined from the experiment are four, since the trace of the matrix is normalized to 1. Equation (B11) is equivalent to Eq. (7) in Sec. III.

Figure 6 shows the fundamental intensities for our present geometry (Figs. 4 and 5). The quantity $I^P_{ss0,t_{0_1}}(F_0)$, for example, shows the line intensity to be observed when the entire population is in the S level. It is zero at $F_0 = 0$ and increases with an increase of $|F_0|$. This is due to the increase in the mixing of the S and P (Fig. 2). In the absence of the field the ratio of the fundamental intensities $I^{\parallel}_{pp0,;t_0t_1}(F_0)$: $I^{\perp}_{pp0;t_0,t_1}(F_0):I^{\parallel}_{pp1;t_0,t_1}(F_0):I^{\perp}_{pp1;t_0,t_1}(F_0)$ is 5:2:4:7. This is simply the result of the coupling of the angular momenta from the uncoupled basis to those in the coupled basis. A calculation shows that the increase of $I^P_{pp0;t_0,tg_1}(F_0)$ and the

decrease of $I^P_{pp1;t_0,t_1}(F_0)$ with an increase of $|F_0|$ are more pronounced when the field disappears more slowly. Thus these dependences are the result of the readjustment of the populations at the boundary: the increase of $I^P_{pp0;t_0,t_1}(F_0)$ stems from the decrease of the decay rate of the Stark mixed P level. The phases of the modulation of both $I^P_{pp0;t_0,t_1}(F_0)$ and $I^P_{pp1;t_0,t_1}(F_0)$ are antiphase to that of $I^P_{ss0,t_{0,1}}(F_0)$. It represents the transfer of the population between the $^2S_{1/2}$ level and mainly the $^2P_{1/2}$ level in the time evolution of the atom.

Since the coherence σ_{sp0} is concerned with the asymmetry of the electron state with respect to the forward and backward direction, its effect is antisymmetric with respect to the change of the direction of the field. The beat of $I^P_{\mathrm{Re}(sp0);t_0,t_1}(F_0)$ is in phase with that of $I^P_{ss0;t_0,t_1}(F_0)$ for positive F_0 and antiphase for negative F_0. The phase difference between the beat of $I^P_{\mathrm{Im}(sp0);t_0,t_1}(F_0)$ and the $I^P_{ss0;t_0,t_1}(F_0)$ is $\pi/2$ or $3\pi/2$.

[1] P. Dobberstein, H. J. Andrä, W. Wittmann, and H. H. Bukow, Z. Phys. **257**, 272 (1972).
[2] M. J. Alguard and C. W. Drake, Phys. Rev. A **8**, 27 (1973).
[3] T. G. Eck, Phys. Rev. Lett. **31**, 270 (1973).
[4] I. A. Sellin, J. R. Mowat, R. S. Peterson, P. M. Griffin, R. Laubert, and H. H. Hasselton, Phys. Rev. Lett. **31**, 1335 (1973).
[5] A. Gaupp, H. J. Andrä, and J. Macek, Phys. Rev. Lett. **32**, 268 (1974).
[6] G. Gabrielse, Phys. Rev. A **23**, 775 (1981).
[7] H. Winter and H. H. Bukow, Z. Phys. A **277**, 27 (1976).
[8] A. Clouvas, M. J. Gaillard, J. C. Poizat, J. Remillieux, A. Denis, and J. Désesquelles, Phys. Rev. A **31**, 84 (1985).
[9] K. Ishii, T. Nakajima, S. Masui, Y. Yoshida, M. Seguchi, and M. Kimura, Z. Phys. D **23**, 55 (1992).
[10] D. L. Harper, R. G. Albridge, N. H. Tolk, W. Qi, D. D. Allred, and L. V. Knight, Phys. Rev. A **52**, 4631 (1995).
[11] H. P. Garnir, Y. Bandinet-Robinet, P. D. Dumont, and A. El Himdy, Z. Phys. D **14**, 45 (1989).
[12] J. Burgdörfer, Z. Phys. A **309**, 285 (1983).
[13] C. C. Havener, N. Rouze, W. B. Westerveld, and J. S. Risley, Phys. Rev. A **33**, 276 (1986).
[14] K. Blum, *Density Matrix Theory and Applications* (Plenum, New York, 1981).